6th **International Conference**
on
Wind Turbine Noise
Glasgow 20-23 April 2015

On the Measurement and Prediction of Wind-Turbine Trailing-Edge Noise

Oksana Stalnov*, Paruchuri Chaitanya, and Phillip F. Joseph

Faculty of Engineering and the Environment,
University of Southampton,
Southampton, Hampshire, SO17 1BJ, UK

Abstract

This paper extends previously published TNO-Blake methods to predict airfoil broadband self-noise due to interaction of a turbulent boundary-layer with a sharp trailing edge. The method presented herein combines Blake's model to predict surface pressure fluctuations and Amiet model to predict trailing edge noise emission. The Blake method is based on the solution of the Poisson equation as an integral of the mean-shear turbulent source interaction, over the entire boundary layer thickness. A recent advances in description of streamwise turbulent intensity are employed to avoid tuning parameters. Surface pressure spectra are measured with remote microphones and compared to the prediction. In the next step, the wavenumber-frequency spectrum as predicted by the TNO model was utilized as an input to the Amiet model to evaluate the far-field trailing edge noise. Agreement between measurements and both predictions are generally within 2 dB.

*o.stalnov@soton.ac.uk

1 Introduction

Wind is a clean and sustainable source of energy. However, a major hindrance to the further adoption of onshore wind-farms is the noise emitted from the wind turbine blades [1]. Wind turbine noise can be divided into mechanical noise, emitted by the gearbox, and flow-induced noise generated by the rotating blades. Mechanical noise can be diagnosed and treated by applying standard engineering methods. Aerodynamic noise, on the other hand, dominates the overall levels and is still being understood at a fundamental level.

Aerodynamic sound is produced by the interaction of the flow with a lifting surface, and may originate from a number of sources, including tip vortices, turbulence of the incoming flow interacting with the blade, and airfoil self-noise. Brooks et al. [2] has identified the following five self-noise mechanisms: turbulent boundary layer trailing edge interactions, the separated boundary layer, the laminar boundary layer vortex shedding, and trailing edge bluntness resulting in vortex shedding noise and tip vortex formation noise. Provided that the lifting surface is not stalled, the most significant source of broadband noise is due to the interaction of the turbulent boundary layer with the trailing edge.

The unsteady pressure developed beneath a turbulent boundary layer on the wall is referred to the blocked pressure. It is twice the pressure that a nominally identical flow would produced if the wall was absent [3]. In the analysis in this paper the turbulent boundary layer wall–pressure is expressed in terms of its wave number-frequency spectrum. This consists of two distinctive regions; the acoustic region where wave components propagate at least as fast as the acoustic wave speed and therefore radiate efficiently to the far field, and the convective hydrodynamic region, where wave components convect slower that the acoustic wave speed and therefore do not radiate efficiently to the far field. Pressure fluctuations within the convective region are much greater that the acoustic region. Even though the radiation from this region is inefficient, it becomes the main source of noise upon interaction with surface roughness and/or other discontinuities (ribs, rivets, joints, etc.) at which convective energy is scattered into radiating components with supersonic wave speeds. This is mechanism associated with trailing edge self-noise.

When an airfoil is situated in a quiet (low-turbulence) flow it radiates broadband noise due to turbulent-boundary layer vortical structures developed along the airfoil surface with the trailing edge. Ffowcs-Williams and Hall [4] were the first to recognize this significance of the trailing edge airfoil self-noise. They derived an analytic expression for the far-field noise radia-

tion that showed that the noise intensity depends on the 5th power of flow velocity. While noise emission from a turbulent boundary layer, without a solid boundary, depends on the 8th power of flow velocity [5]. This implies that at low Mach numbers noise production is greatly amplified by the edge of the blade.

The effect of a sharp trailing edge is to scatter pressure fluctuations beneath the turbulent boundary-layer from relatively short hydrodynamic waves that do not radiate to the far-field into acoustic waves that have much longer wavelength. Early predictions of the far-field broadband noise, for example by Chandiramani [6] and Chase [7, 8], make the assumption a semi-infinite rigid-plate. In this formulation the radiated pressure involves calculation of the diffraction of short (U/f) hydrodynamic waves by the sharp edge into sound with larger wavelength (c/f). These early studies make the assumption that the leading edge is sufficiently far upstream of the trailing edge for secondary leading edge interaction to be neglected. While this is a good approximation at sufficiently high frequency, at low frequency the effect of the finite chord, as well as secondary diffraction by the leading edge must be included. The effect of finite chord length was later introduced by Amiet [9, 10], although the effect of secondary interaction by the leading edge were not included. Roger and Moreau [11] included this effect, which they showed was important only at very low frequencies. An alternative approach that takes into consideration the finite chord was proposed by Howe [12], which is consistent with the Amiet formulation in the low Mach number limit. Despite these later developments the approximation of semi-infinite chord is still widely used. In the low frequency limit the airfoil chord becomes acoustically compact and the radiation directivity is of classical lift dipole type, $sin^2(\theta)$. As the frequency increases, main lobes are introduced and tent towards the limiting pattern $sin^2(\theta/2)$ of a semi-infinite half-plane.

Since the source of airfoil trailing edge self-noise is the turbulent boundary layer an accurate description of its statistical characteristics close to the trailing edge just before it convects over the trailing edge is essential. In the form of solution investigated in this paper knowledge of the surface pressure wavenumber-frequency spectra is required at a position close to the trailing edge, but not too close such that the surface pressure is affected by back scattering of incident waves by the trailing edge. The prediction of the wall pressure fluctuations beneath a turbulent boundary layer on a flat plate was first treated by Kraichnan [13] from solutions of the Poission equation, which governs the relationship between the fluctuating pressure and velocity through the boundary layer. The solution to Poisson's equation implies that pressure at the airfoil surface due to the turbulent boundary is affected by turbulent velocity fluctuation across the entire boundary layer. Smaller

eddies situated close to the inner region of the boundary are generally responsible for high frequency fluctuation while the large eddies situated in the outer region are responsible for the lower frequencies. A widely used model to describe the surface pressure fluctuations based on the solution to Poisson's equation has come to be referred to as the TNO model, which was developed from the work of Blake [14] and later extended by Parchen [15]. The original TNO model, and most other version of this approach, make the assumption of a semi-infinite plane and is therefore only valid in the high frequency limit [16, 8].

The TNO-Blake model has been studied in detail by the Institute of Aerodynamics and Gas Dynamics (IAG) research group [17, 18, 19]. The boundary layer parameters required by the model were measured at the trailing edge of large scale airfoil models in the closed-section laminar wind-tunnel at the IAG. Far-field noise was estimated based on the coherent particle velocity at two hot wire probes in order to reject background noise in the closed tunnel [20]. These measurements, led to the conclusion that the original assumption of local isotropy in the turbulent boundary layer was incorrect and the TNO-Blake model was further modified to include anisotropy in which the turbulence intensity and integral length-scale were allowed to be different in the three orthogonal directions [17]. Anisotropy was introduction through the introduction of 'stretching' coefficients in order to vary the ratios between streamwise and transverse mean square velocities and length-scales. Recent work of Bertagnolio et al. [21] revisited the original model derivation by Blake [14] and discuss the effect of pressure gradient in the estimation of the surface pressure fluctuations and by considering a frequency-dependent vertical correlation length. The introduction of anisotropy by these authors provided much better predictions of the surface pressure and far field noise spectrum. However, all of this work required the stretching coefficients to be 'tuned' by adjusting them to give best fit to the data. One of the innovations of the present work is that this empiricism is avoided by employing stretching coefficients consistent with classical values for a fully turbulent boundary layer.

In this paper we propose a number of modification to the TNO-Blake model with the main objective of removing adjustable empirical constants. Model predictions are compared against surface pressure and far field noise spectra measured in an open jet facility at the University of the Southampton. The main innovations in the model are summarised herein: (1) the well ratios between mean square velocities and length-scale for a fully turbulent boundary layer are chosen thereby removing the requirement for empirical tuning parameters; (2) the effect of finite length of the airfoil chord we incorporate Amiet [9] radiation formula to describe the radiation of sound to the

far-field; (3) Recent developments in describing turbulent layer intensities as a function of the mean profile incorporating and validating. The model will also be assessed in comparison to integral boundary-layer parameters predicted with empirical functions and XFOIL code [22] panel method.

We begin with describing the experimental apparatus used to measure surface pressure, boundary layer profiles and far field noise by a NACA0012 airfoil in an open jet wind tunnel facility in §2. The formulation of the broadband trailing edge noise model is derived in §3. Validation of the boundary-layer parameters modelling is presented in §4, and evaluation of the surface point spectra and far-field noise are presented in section §5. Finally, we discuss the findings significance and error in the comparison between prediction and measurement and conclude in section §7 with discussions of the results and inherent weaknesses in the formulation.

2 Experimental apparatus

In this section we describe the aerodynamic and aeroacoustic measurements that were conducted at the open-jet facility at the Institute of Sound and Vibration Research (ISVR) for the purpose of validating the self-noise prediction model.

Experimental set-up

Free-field measurements of the self-noise of a NACA-0012 airfoil section were made in the open free-jet anechoic wind-tunnel facility at the ISVR. The size of the anechoic chamber is 9.15× m ×9.15 m × 7.32 m. The walls of the chamber are acoustically treated with glass-wool wedges to approximate free-field conditions above about 80 Hz. The wind-tunnel nozzle exit is of rectangular cross-section with dimensions of 0.15 m in height and 0.45 m in width. With this nozzle, the wind-tunnel can reach speeds as high as $U_\infty = 100\,\mathrm{m/s}$. Within the potential core the flow turbulence intensity is less than 0.1%. Background noise levels are generally low except at very low frequencies, typically less than a few 100 Hz, due to turbulent mixing in the jet. A more detailed description of this facility and its characteristics can be found in Chong et al. [23, 24].

To ensure two-dimensionality of the flow field the NACA-0012 airfoil section was positioned horizontally between two end plates, which are rigidly attached to the nozzle. The airfoil leading-edge was located 0.145 m downstream of the nozzle exit which is well within the potential core of the jet. The NACA-0012 airfoil under investigation here has a chord of $c = 0.2\,\mathrm{m}$

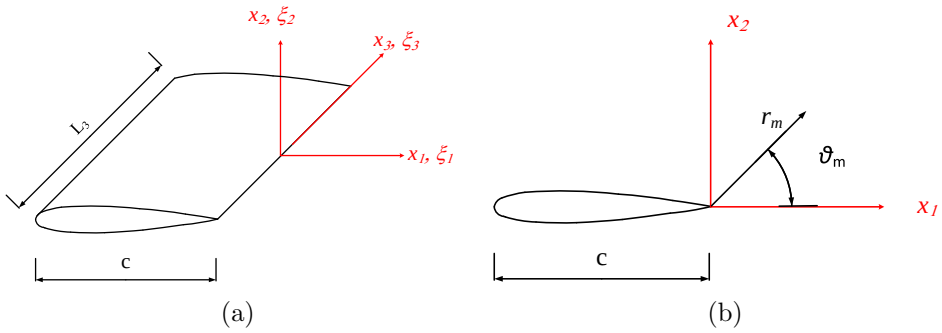

Figure 1: Schematic of the airfoil and the coordinate system.

and span of $L_3 = 0.45\,\mathrm{m}$. The four wind speeds under the investigation here are $U_\infty = 20\,\mathrm{m/s}$, $40\,\mathrm{m/s}$, $60\,\mathrm{m/s}$, and $80\,\mathrm{m/s}$, corresponding to a chord based Reynolds number $Re_c = \frac{U_\infty c}{\nu}$ and Mach number $M = \frac{U_\infty}{c_0}$ in the range $2.6 \times 10^5 < Re_c < 2.6\times < 10^6$ and $0.06 < M < 0.23$, respectively, where ν is the kinematic viscosity and c_0 is the speed of sound.

In order to prevent instability noise from the trailing edge, the flow at $-0.82 < x_1/c < -0.76$ of NACA-0012 model was tripped using a roughness strip on both suction and pressure sides to ensure fully developed turbulent boundary layer. The origin of the coordinate system is in the mid-span x_3 of the trailing edge, as shown in Figure 1(a). The x_1-axis is in the direction of the mean flow and the x_2-axis is in the wall-normal direction.

Model instrumentation and aeroacoustic measurements

For the measurement of surface pressure fluctuations near the trailing edge the airfoil section was instrumented with remote microphone. Microphones are connected to a surface pinhole by a tube that runs from the pressure tap along an inner passage through a T-junction in which a miniature microphone is inserted. The other end of the T-junction is sealed in the end of a long (about 3m long) tube to avoid reflections. The unsteady surface pressure measurements were performed with microphones FG-3329-P07 from Knowles Electronics that are 2.5 mm diameter omnidirectional electret condenser microphones. The microphone calibration was made *in-situ* by comparing their frequency response to the equivalent response of a reference B&K 1/2″ condenser microphone.

Free-field noise measurements were acquired with a microphone array comprising 11 free-field B&K 1/2″ condenser microphones (model 4189) with pre-amplifiers (model 2669) situated over an arc outside the jet shear-layers at

a radial distance from the airfoil mid-chord origin of 1.18 m. The microphones were positioned at an angular range of $40° < \theta_m < 140°$ every 10°. The angle of radiation θ_m is referenced to the direction of the incident flow with the origin at the trailing edge, shown in Figure1(b).

A correction to propagation angle and amplitude due to shear-layer refraction was applied according to Amiet [25]. The microphones were calibrated *in-situ* using a $B\&K - 4231$ Sound Calibrator at a frequency of 1 kHz. The data were sampled using a 24bit National Instruments data acquisition system at a frequency of 50 kHz for a sample period of 10 seconds. The far-field and surface pressure fluctuations are normalized relative to $P_{ref} = 20 \times 10^{-6}$ Pa.

Hot-wire anemometry

Boundary-layer velocity profiles were acquired with hot-wire anemometry. A single hot-wire probe (Dantec type 55P11) was driven using a standard constant temperature anemometry bridge (AA Lab System) operated at an overheat ratio of 1.5. The hot-wire sensor was calibrated in the free-stream against a standard Pitot tube. The calibration function applied was a third-order polynomial that was fit to the calibration data pairs (including the voltage at zero velocity). The preliminary wall position of the sensing element was obtained optically and was adjusted by fitting the near-wall data to a prescribed mean velocity distribution. To ensure convergence of mean statistics the signals were acquired for a period of 60 seconds at sampling frequency of 20 kHz. Hot-wire data was acquired at two free-stream speeds of $U_\infty = 20$ m/s and 40 m/s.

3 Formulation of the broadband trailing edge noise model

Far-field power spectral density

The prediction of broadband acoustic pressure radiated to the far-field from a stationary airfoil of chord c and span L_3 in a uniform streamwise speed U_∞ was considered by Amiet [9]. This theory links the radiated far-field power spectral density of the acoustic pressure $S_{pp}(x_1, x_2, x_3 = 0, \omega)$ to the wall pressure wavenumber-frequency spectrum $\mathscr{P}_w(k_1, k_3, \omega)$ in the vicinity of the trailing edge.

Under the assumption of a large span, the general expression for S_{pp} at

frequency ω for an observer positioned in the mid-span ($x_3 = 0$) is given by

$$S_{pp}(x_1, x_2, x_3 = 0, \omega) = \left(\frac{\omega c x_2}{4\pi c_0 \sigma^2}\right)^2 \frac{\pi L_3}{2} \int_{-\infty}^{\infty} |\mathscr{L}(k_1, k_3 = 0, x_1, x_3, U_\infty, \bar{U}_c)|^2 \hat{\mathscr{P}}_w(k_1, k_3 = 0, \omega) \mathrm{d}k_1 \quad (1)$$

where c_0 is the speed of sound, and k_1 and k_3 are the streamwise and spanwise wavenumbers, respectively, $\sigma^2 = x_1^2 + \beta^2 x_2^2$ is the flow corrected radial distance, with $\beta^2 = 1 - M^2$. Here $\bar{U}_c$ represents the effective convection speed of the boundary layer flow over the airfoil surface and is the net result of eddies of different size convecting at different speeds across the boundary layer.

In this formulation the boundary layer is characterised in terms of the wavenumber-frequency spectrum of the wall pressure close to the trailing edge. It can be determined by the Fourier transform of the corresponding spatial and temporal correlation function $R(\xi_1, \xi_3, \tau)$ defined by

$$\mathscr{P}_w(k_1, k_3, \omega) = \frac{1}{(2\pi)^3} \iiint_{-\infty}^{\infty} R(\xi_1, \xi_3, \tau) e^{-i(k_1\xi_1 + k_3\xi_3 + \omega\tau)} \mathrm{d}\xi_1 \mathrm{d}\xi_3 \mathrm{d}\tau \quad (2)$$

or via the Inverse Fourier Transform

$$R(\xi_1, \xi_3, \tau) = \iiint_{-\infty}^{\infty} \mathscr{P}_w(k_1, k_3, \omega) e^{i(k_1\xi_1 + k_3\xi_3 + \omega\tau)} \mathrm{d}k_1 \mathrm{d}k_3 \mathrm{d}\tau \quad (3)$$

where (ξ_1, ξ_3) represent streamwise and spanwise coordinates confined to the plane of the airfoil boundary surface. The space-time correlation of the wall pressure fluctuating component is defined by

$$R(\xi_1, \xi_2, \tau) = \langle p_w(x_1, x_3, t) p_w(x_1 + \xi_1, x_3 + \xi_3, t + \tau) \rangle \quad (4)$$

where the angle brackets $\langle ... \rangle$ denote time or ensemble average. The term $\mathscr{L}(k_1,\ k_3 = 0,\ x_1,\ x_3, U_\infty, \bar{U}_c)$ is the acoustically weighted unsteady lift function over the surface x_1 and x_3 due to an impinging turbulence with wavenumber k_1 and k_3, defined according to Refs. [9, 10, 26]

$$|\mathscr{L}| = \frac{1}{\theta} \left| (1+i) \left\{ \sqrt{\frac{1 + M + \bar{K}_{x_1}/\mu}{1 + \frac{x_1}{\sigma}}} E^*[2\mu(1 + \frac{x_1}{\sigma})] e^{-i2\theta} - E^*[2((1+M)\mu + \bar{K}_{x_1})] \right\} + 1\} \right| \quad (5)$$

where

$$\theta = \bar{K}_{x_1} + \mu\left(M - \frac{x_1}{\sigma}\right), \quad \bar{K}_{x_1} = \omega/\bar{U}_c, \quad \mu = \frac{M\omega b}{U\beta^2} \tag{6}$$

and $E^*(x)$ represents the complex Error function

$$E^*(x) = \int_0^x \frac{e^{-i\xi_0}}{\sqrt{2\pi\xi_0}} \mathrm{d}\xi_0 \tag{7}$$

and is deduced in practice from a combination of Fresnel integrals.

It should be noted that the Amiet model was recently extended by Roger and Moreau [11] to take into the account secondary scattering of sound by the leading-edge. The back-scattering leading-edge correction is found partially to cancel the contribution from the main trailing edge term at low acoustic wavenumbers $k_0 = \omega/c_0$ and it vanishes in the high frequency limit $k_0 c \to \infty$.

For frozen turbulence the streamwise wavenumber is equal to $k_1 = \omega/\bar{U}_c$, and Eq.(1) takes the form

$$S_{pp}(x_1, x_2, x_3 = 0, \omega) = \left(\frac{\omega c x_2}{4\pi c_0 \sigma^2}\right)^2 \frac{\pi L}{2\bar{U}_c} \\ |\mathscr{L}(\omega/\bar{U}_c, k_3 = 0, x_1, x_3, U_\infty, \bar{U}_c)|^2 \mathscr{P}_w(\omega/\bar{U}_c, k_3 = 0, \omega). \tag{8}$$

Modelling wavenumber-frequency spectra of surface pressure

Poisson equation for a turbulent shear-flow

The wall pressure fluctuations beneath an incompressible turbulent boundary layer are governed by the Poisson equation [13, 14], which is derived by taking the divergence of the Navier-Stokes [27, 28] equation and then using the continuity equation to drop terms. By performing Reynolds decomposition of the flow and subtracting the mean equation from the equation involving fluctuating quantities, we can obtain the following relation for the fluctuating pressure

$$\nabla^2 p = q(\xi_1, \xi_2, \xi_3, t) \tag{9}$$

where

$$q(\xi_1, \xi_2, \xi_3, t) = -2\rho \frac{\partial u_j}{\partial x_i}\frac{\partial U_i}{\partial x_j} - \frac{\partial^2}{\partial x_i \partial x_j}(u_i u_j - \overline{u_i u_j}) \tag{10}$$

Here ρ is the fluid density, and u_i and p are the velocity and pressure fluctuations, respectively. Upper case symbols denote the mean quantities and the lower case symbols denote fluctuating quantities, where overbar $\bar{}$ denotes the time average.

The first source term on the right hand side of Eq.(10) is due to turbulence interactions with the mean-shear (MS); the second term represents turbulence-turbulence (TT) interactions. In shear-flows, the MS turbulence interactions are generally an order of magnitude higher than the TT interactions [13]. Adopting the standard boundary layer approximation, whereby the mean streamwise velocity component $U_1(x_2)$ is assumed to vary only in the x_2 direction (normal to the wall), and applying the continuity equation for the fluctuating velocity $\partial u_i/\partial x_i = 0$, yields the source term $q(\xi_1, \xi_2, \xi_3, t)$ in Poisson equation which now simplifies to

$$q(\xi_1, \xi_2, \xi_3, t) = -2\rho \frac{dU_1}{dx_2}\frac{\partial u_2}{\partial x_1} \tag{11}$$

where dU_1/dx_2 denotes the mean-shear and u_2 is the velocity component normal to the airfoil surface.

Spectral solution of the Poisson equation

The solution to the Poisson Eq.(11) in free space can be expressed as the convolution of the source terms $q(\xi_1, \xi_2, \xi_3, t)$ and the free field Green function integrated over the fluid volume $V(\mathbf{y})$

$$p(x_1, x_2, x_3, t) = \iiint\limits_{\infty}^{\infty} \frac{q(\xi_1, \xi_2, \xi_3, t)}{4\pi|\mathbf{x} - \xi|} \mathrm{d}\, V(\xi) \tag{12}$$

The wall boundary condition on the rigid wall surface, $\partial p_w/\partial x_2 = 0$, can be treated using the method of images, where the pressure p_w, which develops beneath a turbulent boundary layer on the wall, is twice the pressure that would be produced by a nominally identical flow in the absence of the wall [3]. The solution for the surface pressure is now modified as,

$$p_w(x_1, x_3, t) = \int\limits_{0}^{\infty} \mathrm{d}\xi_2 \iint\limits_{-\infty}^{\infty} \frac{q(\xi_1, \xi_2, \xi_3, t)}{2\pi r} \mathrm{d}\xi_1 \mathrm{d}\xi_3. \tag{13}$$

where $r = \sqrt{(x_1 - \xi_1)^2 + \xi_2^2 + (x_3 - \xi_3)^2}$. It is convenient to solve Eq.(13) in terms of spectral variables [29, 30] and hence obtain the solution for the pressure wavenumber-frequency spectrum, which is simply the time-space Fourier transform of $p_w(x_1, x_2, x_3, t)$

$$\hat{p}_w(k_1, k_3, \omega) = \frac{1}{(2\pi)^3} \iiint\limits_{-\infty}^{\infty} p_w(x_1, x_3, t) e^{-i(k_1 x_1 + k_3 x_3)} e^{i\omega t} \mathrm{d}x_1 \mathrm{d}x_3 \mathrm{d}t. \tag{14}$$

Substituting Eq.(13) into Eq.(14) yields an expression containing six integrals that may be simplified by changing the orders of integration, so that the integration over the 1, 3 plane is performed first. Provided that each layer is sufficiently large, the surface integral is straightforward [31] using the Fourier Transform of r^{-1} and the definition of Dirac delta function

$$\frac{1}{2\pi}\iint_{-\infty}^{\infty}\frac{e^{-i(k_1x_1+k_3x_3)}}{r}\mathrm{d}x_1\mathrm{d}x_3=\frac{e^{-k\xi_2}}{k}e^{-i(k_1\xi_1+k_3\xi_3)} \tag{15}$$

where $k=\sqrt{k_1^2+k_3^2}$ is the magnitude of the wavenumber.

$$\hat{u}_2(k_1,x_2,k_3,\omega)=\frac{1}{(2\pi)^3}\iiint_{-\infty}^{\infty}u_2(x_1,x_2,x_3,t)e^{i(k_1x_1+k_3x_3)}e^{i\omega t}\mathrm{d}x_1\mathrm{d}x_3\mathrm{d}\omega \tag{16}$$

where $u_2(k)$ is the wavenumber spectrum of vertical velocity component $u_2(x_1,x_2,x_3,t)$ through the boundary layer. Recalling the differential property of $\partial u_2/\partial x_1$ is equal to $k_1\hat{u}_2(k_1,x_2,k_3,\omega)$ in the Fourier transform, the spectral solution of the surface pressure may be obtained as

$$\hat{p}_w(k_1,k_3,\omega)=-2\rho\int_0^{\infty}\frac{\partial U_1}{\partial x_2}\frac{k_1}{k}\hat{u}_2(k_1,x_2,k_3,\omega)e^{-x_2k}\mathrm{d}x_2 \tag{17}$$

Since broadband trailing edge noise is a stochastic phenomenon, it is useful to work with pressure wavenumber-frequency spectral densities. and hence obtain the solution for the pressure wavenumber-frequency spectrum, which is simply that the turbulent pressure field and velocity field $u_2(x_2)$ are spatially homogeneous (i.e., its correlation function only depends on separation distance) and stationary with respect to time. Under these assumptions

$$\mathscr{P}_w(k_1,k_3,\omega)\delta(k_1-k_1')\delta(k_3-k_3')\delta(\omega_1-\omega_1')= \langle\hat{p}_w(k_1,k_3,\omega)\hat{p}_w^{\star}(k_1',k_3',\omega')\rangle \tag{18}$$

and

$$\phi_{22}(k_1,x_2,x_2',k_3,\omega)\delta(k_1-k_1')\delta(k_3-k_3')\delta(\omega_1-\omega_1')= \langle\hat{u}(k_1,x_2,k_3,\omega)\hat{u}^{\star}(k_1',x_2',k_3',\omega')\rangle \tag{19}$$

where $\star$ represents the complex conjugate, and δ is the Dirac delta function.

The multiplication of the amplitude spectrum and its subsequent averaging yields an expression which needs to be integrated twice with respect to the independent coordinates x_2 and x_2' . Combining Eq.(17) with Eq.(18) yields an expression for the wavenumber-frequency spectrum of the surface pressure fluctuations

$$\mathscr{P}_w(k_1,k_3,\omega) = 4\rho^2\frac{k_1^2}{k^2}\int_0^\delta \mathrm{d}x_2\int_0^\delta \mathrm{d}x_2'\sqrt{\overline{u_2^2}(x_2)\overline{u'^2_2}(x_2')}\frac{\partial U_1(x_2)}{\partial x_2}\frac{\partial U_1(x_2')}{\partial x_2}$$
$$\tilde{\phi}_{22}(k_1,x_2,x_2',k_3,\omega)e^{-|k|(x_2+x_2')} \quad (20)$$

where $\tilde{\phi}_{22}(k_1,x_2,x_2',k_3,\omega)$ is the cross-spectral density of the vertical velocity fluctuations. Finally, we make the approximation to $\tilde{\phi}_{22}(k_1,x_2,x_2',k_3,\omega)$ that was first introduced by Blake [14] and Parchen [15], which essentially separates the various spatial and wavenumber components according to

$$\tilde{\phi}_{22}(k_1,x_2,x_2',k_3,\omega) = \Lambda_{2|22}(x_2)\delta(x_2-x_2')\overline{u_2^2}(x_2)\phi_{22}(k_1,k_3)\phi_m(\omega-U_c(x_2)k_1) \quad (21)$$

where $\Lambda_{2|22}(x_2)$ is the vertical integral length scale, $\phi_{22}(k_1,k_3)$ is the dimensionless energy density of the vertically directed velocity fluctuations, and $\phi_m(\omega-U_c(x_2)k_1)$ is the moving axis spectrum that describes how the $\phi_{22}(k_1,k_3)$ spectrum of the vertical velocity fluctuations is distorted as a result of the generation and distortion of the eddies during the convection over the trailing edge at a convection speed $U_c(x_2)$. Integration of Eq.(18) with respect to x_2' yields the final expression for the of the wall pressure wavenumber-frequency spectral density

$$\mathscr{P}_w(k_1,k_3,\omega) = 4\rho^2\frac{k_1^2}{k^2}\int_0^\delta \Lambda_{2|22}(x_2)\left(\frac{\partial U_1(x_2)}{\partial x_2}\right)^2$$
$$\overline{u_2^2}(x_2)\phi_{22}(k_1,k_3)\phi_m(\omega-U_c(x_2)k_1)e^{-2|k|x_2}.\mathrm{d}x_2 \quad (22)$$

Point Frequency Spectrum and Spanwise Correlation Length

The largest contribution to $\mathscr{P}_w(k_1,k_3=0,\omega)$ arises from the streamwise turbulence wavenumber components k_1 in the vicinity of the convective ridge. We now make the usual assumption of 'frozen' turbulence where turbulence is assumed to convect unchanged as it passes over the trailing edge. In this case the streamwise wavenumber at any location in the boundary layer x_2 takes the form $k_1 = \omega/U_c(x_2)$, where $U_c(x_2)$ is the local mean convection

velocity. Thus, under the 'frozen' turbulence assumption the moving axis spectrum can be simplified to

$$\phi_m(\omega - U_c(x_2)k_1) = \delta(\omega - U_c(x_2)k_1). \tag{23}$$

The validity of this assumption was previously demonstrated by several authors where it was shown that it gives similar results to a Gaussian function of finite temporal correlation time [21].

In order to predict surface pressure spectra the frequency-wavenumber spectrum defined in Eq.(22) is integrated over all wavenumber components k_1 and k_3. After making the frozen gust assumption the integral over k_1 yields the delta function as defined in equation. The surface pressure frequency spectrum can be obtained by integrating equation Eq.(22) over k_3 which can be approximated by the introduction of the spanwise correlation length

$$\Pi(\omega) = \frac{\pi}{U_c}\frac{1}{\Lambda_{p|3}}\mathscr{P}_w(k_1 = \omega/U_1(x_2), k_3 = 0) \tag{24}$$

where the spanwise frequency-dependent correlation length $\Lambda_{p|3}(\omega)$ is given by

$$\Lambda_{p|3}(\omega) = \int_0^\infty \sqrt{\gamma^2(\omega, \Delta\xi_3)}d(\Delta\xi_3) \tag{25}$$

where $\gamma^2(\omega, \Delta\xi_3)$ is coherence function between two microphones separated spanwise distance $\Delta\xi_3$

$$\gamma^2(\omega, \Delta\xi_3) = \frac{\langle p_w(x_1, x_2 = 0, x_3, \omega)p_w^\star(x_1, x_2 = 0, x_3 + \Delta\xi_3, \omega)\rangle}{p_w(x_1, x_2 = 0, x_3, \omega)p_w(x_1, x_2 = 0, x_3, \omega).} \tag{26}$$

The product on the right hand side of Eq.(24) is precisely the source term in Eq.(1) of Amiet's broadband trailing edge model. The point wall pressure frequency spectrum $\Pi(\omega)$ may be measured by a single pressure transducer on the airfoil surface and the spanwise correlation length $\Lambda_{p|3}(\omega)$ can be estimated from the coherence measurements between the surface pressure at a finite number of lateral spanwise points. It should be noted that in the case of a curved surface such as an airfoil, the precise value of $\Lambda_{p|3}(\omega)$ can be different from the one presented in Eq.(25).

Combining Eqs.(24) and (23) and utilizing the sifting property of the Dirac delta function we may write,

$$\int_{-\infty}^{\infty} f(k_1)\delta(\omega - U_c(x_2)k_1)\mathrm{d}k_1 = \frac{1}{U_c(x_2)}f\left(\frac{\omega}{U_c(x_2)}\right) \tag{27}$$

which allows Eq.(22) to be further simplified to

$$\Pi(\omega) = \frac{4\pi\rho^2}{\Lambda_{p|3}(\omega)} \int_0^\delta \Lambda_{2|22}(x_2) U_c(x_2) \left[\frac{\partial U_1(x_2)}{\partial x_2}\right]^2 \frac{\overline{u_2^2}(x_2)}{U_c^2(x_2)} \phi_{22}(\omega/U_c(x_2), k_3 = 0) e^{-2|k|x_2} \mathrm{d}x_2. \quad (28)$$

Note that in Eq.(28) we have introduced a factor of 2 to recognise the fact that the point spectrum $\Pi(\omega)$ is symmetric about $x_2 = 0$.

4 Evaluation of boundary layer parameters

In the current work the terms introduced in Eq.(28) are estimated with the XFOIL code [32] and empirical boundary-layer functions. Examples of some well-known prediction codes that utilize the XFOIL code include NAFNoise [33], RISO-XFOIL [34, 35], Xnoise [19, 36, 37, 38, 17]. The XFOIL code is a panel method that provides boundary-layer integral properties, such as displacement δ^* and momentum θ thickness, and skin friction coefficient. However, the code does not provide direct information about the wall-normal thickness or velocity profiles, which is essential for the evaluation of the source terms in the prediction model described by Eq.(28).

Mean-shear

The mean-shear term $\partial U_1/\partial y_2$ can be modelled with the log-wake law [39]. The law of the wall is an empirically-determined relationship governing the behaviour of turbulent flows near solid boundaries. The streamwise velocity $U_1(x_2)$ outside the viscous-dominated near-wall region is a sum of a logarithmic part and a wake component. The variation of the normalized mean velocity $U_1^+ = U_1(x_2)/u_\tau$ with normalized distance from the wall $x_2^+ = x_2 u_\tau/\nu$ is therefore described by

$$U_1^+(x_2) = k^{-1} \ln x_2^+ + B + \frac{2\Pi_w}{k} \sin^2\left(\frac{\pi x_2}{2\delta}\right), \quad (29)$$

where u_τ is the friction velocity, and k and B are the von-Kármán and an additive empirical constants, respectively. There is much debate over the exact empirical constants, here empirical values of k and B are 0.38 and 5, respectively. The friction velocity $u_\tau = \sqrt{\tau_w/\rho}$ can be defined with the local shear stress τ_w, which is estimated with the XFOIL code via the local skin friction coefficient $C_f = \tau_w/0.5\rho U_\infty^2$.

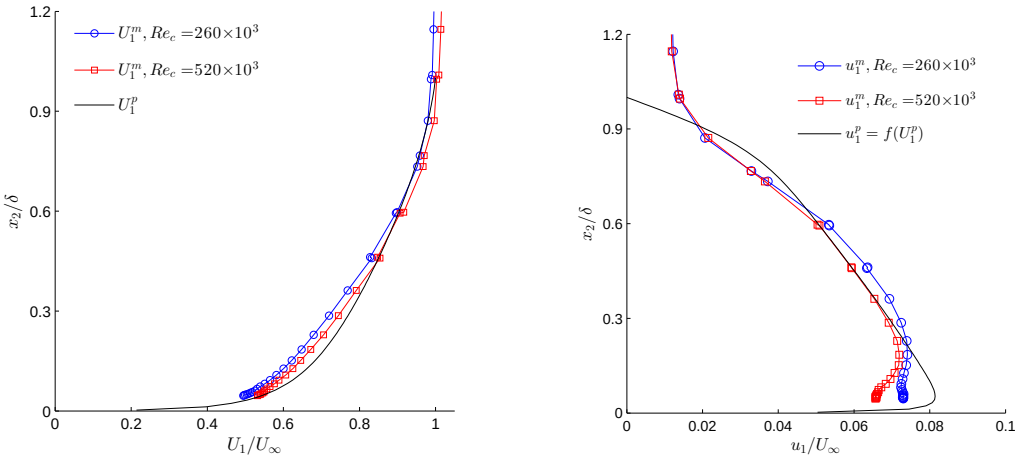

(a) (b)

Figure 2: Measured and predicted streamwise (a) mean and (b) turbulent intensity profiles over the NACA-0012 airfoil section at $Re_c = 260 \times 10^3$ and 520×10^3. The measured velocity profile were acquired at $x/c = -0.025$. Superscripts m and p indicate measured and predicted profiles.

The last term in Eq.(29) is the Coles's [39] wake function, as defined by Hinze [40]. It takes into the account the effect of adverse pressure gradient on the mean streamwise velocity component. The pressure gradient parameter $\Pi_w = 0.8(\beta + 0.5)^{3/4}$ is a function of the local pressure gradient dC_p/dx_1 and wall shear stress τ_w, with $\beta = \delta^*/\tau_w dC_p/dx_1$. The boundary layer thickness may be estimated from the following empirical relation suggested by Drela [22] can be applied

$$\delta = \theta \left(3.15 + \frac{1.75}{H-1}\right) + \delta^* \tag{30}$$

where $H = \delta^*/\theta$ is a kinematic shape factor.

A comparison between the measured and predicted streamwise mean and turbulent intensity velocity profiles measured upstream of the trailing edge of a NACA-0012 airfoil at two flow speeds $U_\infty = 20\,\mathrm{m/s}$ and $40\,\mathrm{m/s}$ (corresponding to $Re_c = 260 \times 10^3$ and $Re_c = 520 \times 10^3$) is shown in Figure 2. The boundary layer profiles were measured at $x/c = -0.025$. Distance from the airfoil surface was estimated with digital photography by setting it as half the distance from the wire to its image, as reflected in the polished wall surface. The thickness of tripped boundary layer for both flow speeds was in order of $\delta \approx 10\,\mathrm{mm}$,which is in agreement with the the measurements reported by Sagrado [41]. Estimated boundary layer profile with Eq.(29)is

plotted for reference. Note that the boundary layer near the trailing edge is subject to an adverse gradient and is not fully developed.

Turbulence intensities

Eq.(28) for airfoil surface pressure spectrum and Eq.(1) for self-noise requires the variation of turbulence intensity normal to the airfoil $u_2(x_2)/U_\infty$ direction. However, in practice the measurement of the velocity in the normal direction is not straightforward due to relatively large physical size of x-wire probe, compared to the thickness of the boundary layer. Kamruzzaman et al. [17] estimated the wall normal intensity using the Prandtl's mixing-layer hypothesis. However, this approach fails to predict the fluctuation level and the maximum location in the near wall region.

In this paper we set the ratios of mean square velocity to those of an incompressible zero pressure gradient boundary-layer, i.e. in the following empirical ratios $\overline{u_2^2} = \frac{1}{2}\overline{u_1^2}$ and $\overline{u_3^2} = \frac{3}{4}\overline{u_1^3}$ [42]. These ratios are of course not constant throughout the boundary layer and might be influenced by the local pressure gradient. However, they are usually reckoned to be a good approximation [43, 44] provided the pressure gradient is not significant and the boundary-layer remains attached.

One of the main contributions of this paper is the use of recent work of Alfredsson et al. [45, 46] to estimate the variation of mean square turbulence velocity. They showed that the streamwise turbulence intensity $u_1(x_2)/U_\infty$ through the boundary layer could simply deduced from the mean streamwise velocity profile. This relationship was found valid starting within the logarithmic layer, and continuing throughout almost the entire outer region. Alfredsson et al. [45, 46] showed that for a zero-pressure gradient boundary-layer the turbulence intensity $u_1(x_2)/U_\infty$ decreases almost linearly with the normalized streamwise velocity component $U_1(x_2)/U_\infty$ according to the following empirical relation

$$\frac{u_1(x_2)}{U_1(x_2)} = \left(a + b\left(\frac{U_1(x_2)}{U_\infty}\right)\right) Q\left(\frac{U_1(x_2)}{U_\infty}\right) \tag{31}$$

where $a = 0.2909$ and $b = -0.2598$ are empirical constants [46]. Note that this linear relation is independent of the Reynolds number. Since the mean streamwise $U_1(x_2)$ velocity approaches the free-stream velocity much faster than $u_1(x_2)$ in the free-stream region, a correction factor is introduced

$$Q\left(\frac{U_1(x_2)}{U_\infty}\right) = 1 - e^{-\gamma(1-U_1(x_2)/U_\infty)} \tag{32}$$

where $\gamma = 64$.

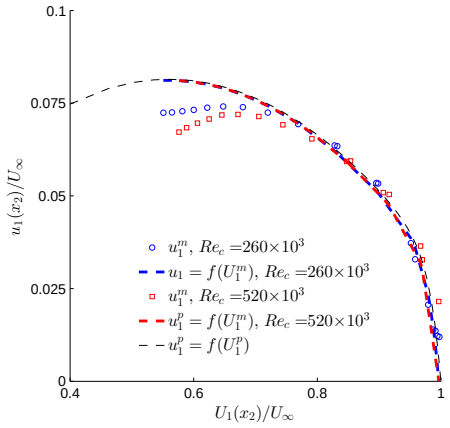

Figure 3: Streamwise turbulent intensity u_1/U_∞ plotted against the streamwise mean velocity. Superscripts m and p indicate measured and predicted profiles. The dashed lines correspond to estimation of u_1/U_∞ based on measured and predicted U_1/U_∞ and Eq.(31)

The Alfredsson relation was verified only for fully developed canonical flows, such as boundary layers and pipe and channel flows, and further verification was required. In the current work this relation was verified with the boundary layer profiles shown in Figure 2. This data is plotted in the form of a diagnostic plot in Figure 3. The streamwise turbulent intensity in the outer region collapses on a straight line as a function of $U_1(x_2)/U_\infty$, independently of Reynolds number. The deviation from a straight line occurs in the inner region, where the appropriate scaling of $u_1(x_2)/U_\infty$ should be replaced with the inner variables U_1/u_τ.

Figure 2(b) shows the measured and predicted streamwise intensity. A typical maximum value of 0.1 is observed in the streamwise intensity profile[41]. The solid line shows the predicted streamwise intensity based on Eq.(31) and mean streamwise boundary layer profile as predicted with Eq.(29). The current data exhibits similar behaviour suggesting that the diagnostic plot may be universal. The significant feature of the diagnostic plot is that both abscissa and ordinate are normalized with the outer velocity U_∞, thereby avoiding any uncertainties in both the wall position and the estimation of the friction velocity u_τ.

Integral length scale

An important distinction needs to be emphasized on the difference between two commonly measured integral length scales. The most commonly integral length scale in traditional turbulence measurement is the longitudinal integral

correlation scale $\Lambda_{11|1}$. However, the important correlation length scale in terms of the acoustic production from an airfoil is the transverse correlation of the normal $\Lambda_{2|22}$

The turbulent vertical integral length scale $\Lambda_{2|22}$ is related to the vertical extent of the turbulent eddies. More precisely, it is defined as the integral of the normalized spatial two-point correlation coefficient $R_{22}(\Delta x_2)$ of the vertical velocity fluctuations.

$$\Lambda_{2|22}(x_2) = \int_0^\delta R_{22}(\Delta x_2)\mathrm{d}(\Delta x_2) = \int_0^\delta \frac{\overline{u_2(x_2)u_2(x_2')}}{\sqrt{u_2^2(x_2)u_2^2(x_2')}}\mathrm{d}(\Delta x_2) \tag{33}$$

where $\Delta x_2 = x_2 - x_2'$. This integral length scale, however, is not easily measured as it requires traversing one x-wire and keeping the other wire in the same location.

When using XFOIL code, the integral length scale is determined by using Schlichting's formula for the mixing length scale [47], and dividing by the von-Kármán constant. Since the mixing length is representative of the size of the turbulent eddies in the boundary layer Parchen [15] suggested to derive $\Lambda_{2|22}$ from mixing length-scale l_{mix}

$$\Lambda_{2|22}(x_2) = \frac{l_{mix}(x_2)}{k}. \tag{34}$$

The application of mixing length theory is representative of the size of the turbulent eddies in the boundary layer.

To derive $\Lambda_{2|2}$ from known quantities, following methods can be applied depending on the aerodynamic simulation methods employed for the noise prediction. This length-scale is further corrected [48] with Klebanoff damping function near the boundary-layer edge. Thus resulting in

$$l_{mix}(x_2) = \frac{0.085\delta \tanh\left(\frac{k}{0.085}\left(\frac{x_2}{\delta}\right)\right)}{\sqrt{1 + B(\frac{x_2}{\delta})^6}}. \tag{35}$$

Velocity spectra

Turbulent flows in reality, such as boundary layers, are neither homogeneous nor isotropic. The anisotropy of the velocity spectra to a large extent, is mostly present in the large scale. Thus, the anisotropy in this paper is introduced in a manner similar to Panton and Linebarger [49] with the anisotropy factors β_1, β_2, β_3, and later used by Kamruzzaman [17] and Bertagnolio [21]. These factors act as stretching parameters to the classic von-Kármán isotropic energy density spectrum. Since in the boundary layer the eddy

structure is elongated in a given direction we assume the following form of two-dimensional normalized vertical velocity spectra $\phi_{22}(k_1, k_3, \beta_1, \beta_3)$ (integrated over k_2)

$$\phi_{22}(k_1, k_3, \beta_1, \beta_3) = \frac{4}{9\pi} \frac{\beta_1 \beta_3}{k_e^2} \frac{(\beta_1 k_1/k_e)^2 + (\beta_3 k_3/k_e)^2}{[1 + (\beta_1 k_1/k_e)^2 + (\beta_3 k_3/k_e)^2]^{7/3}} \tag{36}$$

where k_e is the wavenumber of the main energy bearing eddies that are inversely proportional to the integral length scale, which in turn is strongly related to the boundary layer thickness [16].

For isotropic turbulence, the wavenumber of the main energy bearing eddies can be defined in terms of the longitudinal integral length scale $\Lambda_{11|1}$, using the following definition

$$k_e(x_2) = \frac{\sqrt{\pi}}{\Lambda_{11|1}(x_2)} \frac{\Gamma(5/6)}{\Gamma(1/3)} \tag{37}$$

where Γ is the standard Gamma function. Assuming isotropic relation, the longitudinal length scale is related to the transverse length scale according to $2\Lambda_{2|22}(x_2) = \Lambda_{11|1}(x_2)$.

In this definition the effect of β_i is merely to scale differently the various turbulence wavenumber components in the three orthogonal directions, and not to modify energy content in any way. The degree of anisotropy between two different flow components could be defined by

$$\beta_i = \frac{\overline{u_i^2}}{\overline{u_1^2}}. \tag{38}$$

Unless otherwise stated, the stretching factors assumed to be equal to $\beta_1 = 1$, $\beta_2 = 1/2$, $\beta_3 = 3/4$.

For prediction of the wavenumber-frequency spectrum components contributing to the noise radiated to the far-field and detected by an observer in the mid-plane, the spanwise wavenumber is set to $k_3 = 0$, thus resulting in the following normalized vertical velocity spectrum

$$\phi_{22}(k_1, k_3 = 0, \beta_1, \beta_3) = \frac{4}{9\pi} \frac{\beta_1 \beta_3}{k_e^2} \frac{(\beta_1 k_1/k_e)^2}{[1 + (\beta_1 k_1/k_e)^2]^{7/3}} \tag{39}$$

Note that in prediction of the far-field only the streamwise β_1 and spanwise β_3 anisotropic factors play role in the prediction of $\Phi_{22}(k_1, k_3 = 0, \beta_1, \beta_3)$

In this study we compare measured one dimensional spectra with the anisotropic von-Kármán model given by

$$\phi_{11}(k_1) = \frac{\Gamma(5/6)}{\sqrt{\pi}\Gamma(1/3)} \frac{\beta_1}{k_e} \frac{1}{[1 + (\beta_1 k_1/k_e)^2)^{5/6}} \tag{40}$$

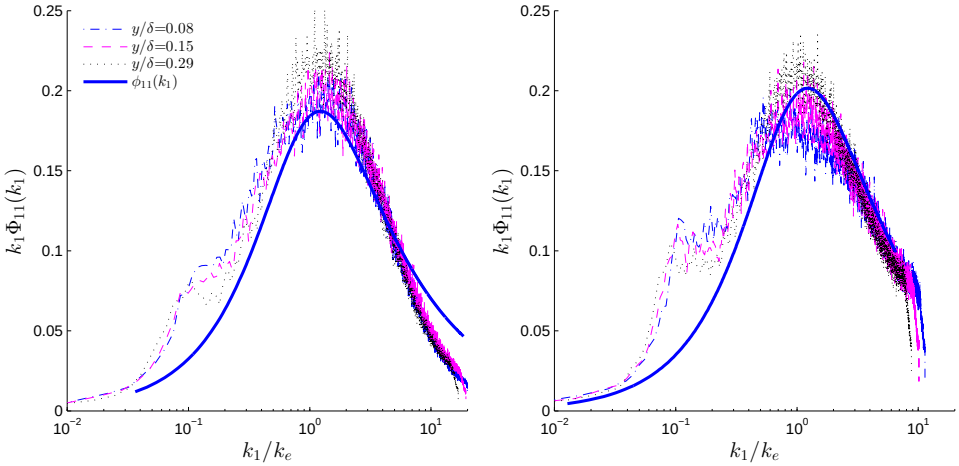

(a) $U_\infty = 20\,\mathrm{m/s}$, $Re_c = 260 \times 10^3$ (b) $U_\infty = 40\,\mathrm{m/s}$, $Re_c = 520 \times 10^3$

Figure 4: Pre-multiplied wavenumber spectra of streamwise velocity component. The von-Kármán wavenumber spectra $\phi_{11}(k_1)$ was defined with Eq.(40).

Figure 4 shows pre-multiplied one dimensional wavenumber spectra $k_1\phi_{11}(k_1)$ of streamwise velocity component for two free-streamwise velocities $U_\infty = 20\,\mathrm{m/s}$ and $40\,\mathrm{m/s}$ (corresponding to $Re_c = 260 \times 10^3$ and $Re_c = 520 \times 10^3$). The plotted spectra are pre-multiplied by the wavenumber k_1 in order to clearly identify the spectrum peak wavenumber k_e. The von-Kármán wavenumber spectra $\phi_{11}(k_1)$ of streamwise velocity component is plotted for reference and it is determined with Eq.(40). The deviation of the predicted spectra from the hot-wire measurements in the low wavenumber range is due to jet noise.

Figure 5 shows comparison of the measured and predicted wavenumber of main energy containing eddies at $Re = 520 \times 10^3$. Prediction of $k_e(x_2)$ is based on Eq.(37). The $k_e(x_2)$ was determined as the local maximum in the pre-multiplied spectra of streamwise velocity component. In vicinity of the wall a clear disagreement between the measured and predicted $k_e(x_2)$ values is observed. However, at increasing distance from the wall the predicted and measured values follow similar trend. The agreement is less good at $20\,\mathrm{m/s}$.

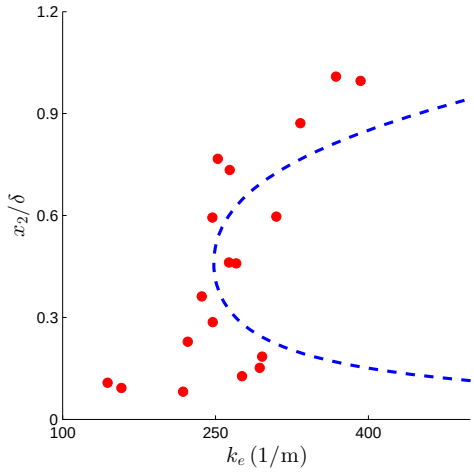

Figure 5: Measured (red dots) and predicted (dashed line) wavenumber of the turbulence energy containing eddies k_e at $Re = 520 \times 10^3$.

5 Evaluation of surface pressure parameters and the model

Surface pressure mean convection velocity

Comparison of the convection velocity measured on different airfoils at the same free stream velocity vary by up to about 20% depending on frequency, local flow velocity and sensor separation distance [41, 50, 9, 16]. It is therefore important to make this measurement in-situ. The average convection velocity between two sensors separated by distance $\Delta\xi_1$ can be deduced from the gradient of the phase spectrum ϕ_{ij} (obtained by least squares fit) according to,

$$\bar{U}_c = \frac{\Delta\xi_1}{\partial\phi_{ij}(\omega)/\partial\omega} \tag{41}$$

where $\Delta\xi_1$ is the streamwise distance between the two microphones.

Figure 6(a) shows phase spectra versus $\omega/\bar{U}_c$ between a pair of remote microphones, after calibration with streamwise separation distance $\Delta\xi_1/c = 0.0620$ at four different flow speeds. The reference sensor located $x_1/c = 0.0225$ upstream of the trailing edge. Only the data up to $\omega/\bar{U}_c = 1000\ \mathrm{m}^{-1}$ is plotted since above this 'frequency' the coherence is poor.

The convection velocity is seen to be insensitive to the chord-based Reynolds number. The grey dotted line indicate the phase difference as estimated by Eq.(41) with $U_c = 0.65U_\infty$, which is consistent with the result from previous airfoil measurement [9, 16] and will be used in Eq.(1) for making airfoil

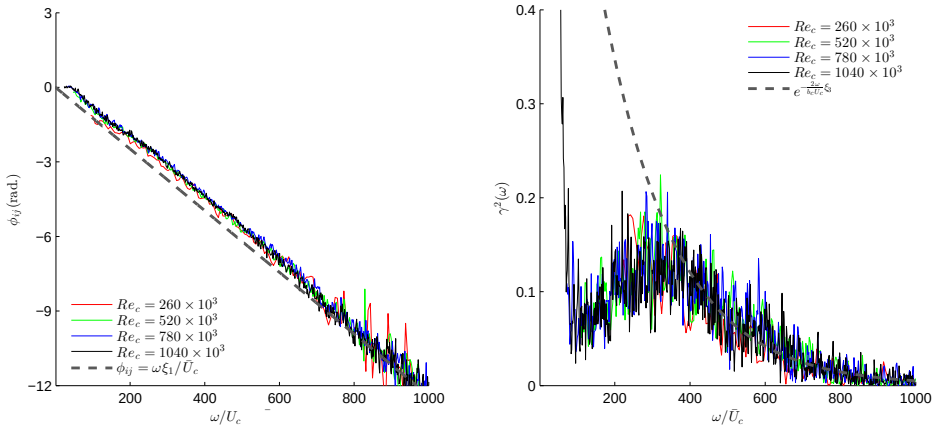

(a) (b)

Figure 6: (a) Mean convection velocity and (b) spanwise correlation length scale as estimated from a pair of streamwise and spanwise microphones. The spanwise microphones positioned $x/c = -0.02$ and separated by spanwise distance $\Delta\xi_3/c$=0.0185.

self-noise predictions.

Spanwise correlation length of wall-pressure fluctuations

Eq.(1) for the prediction of the radiated airfoil self-noise requires the surface pressure frequency-wavenumber spectrum $\mathscr{P}_w(k_1, k_3, \omega)$. Its direct measurement is problematic but may be estimated from Eq.(25) involving the product of the surface pressure spectrum and the spanwise correlation length scale $\Lambda_{p|3}(\omega)$. This is in agreement with Corcos [50] has postulated a model for the coherence function in a turbulent boundary layer of the form

$$\gamma^2(\omega, \Delta\xi_3) = e^{-\frac{2\omega}{b_c\bar{U}_c}\Delta\xi_3} \tag{42}$$

which upon substituting into Eq.(25) yields the theoretical spanwise correlation length scale

$$\Lambda_{p|3}(\omega) = b_c\frac{\bar{U}_c}{\omega}, \tag{43}$$

where $\bar{U}_c$ is the mean convection velocity($\bar{U}_c = 0.65U_\infty$) and $b_c = 1.4$ is the Corcos's constant.

Figure 6(b) present the spanwise correlation length scale for the four Reynolds number tested. The pair of microphones separated spanwise distance of $\Delta\xi_3 = 0.037\,\mathrm{m}$. The experimental data matches the Corcos model

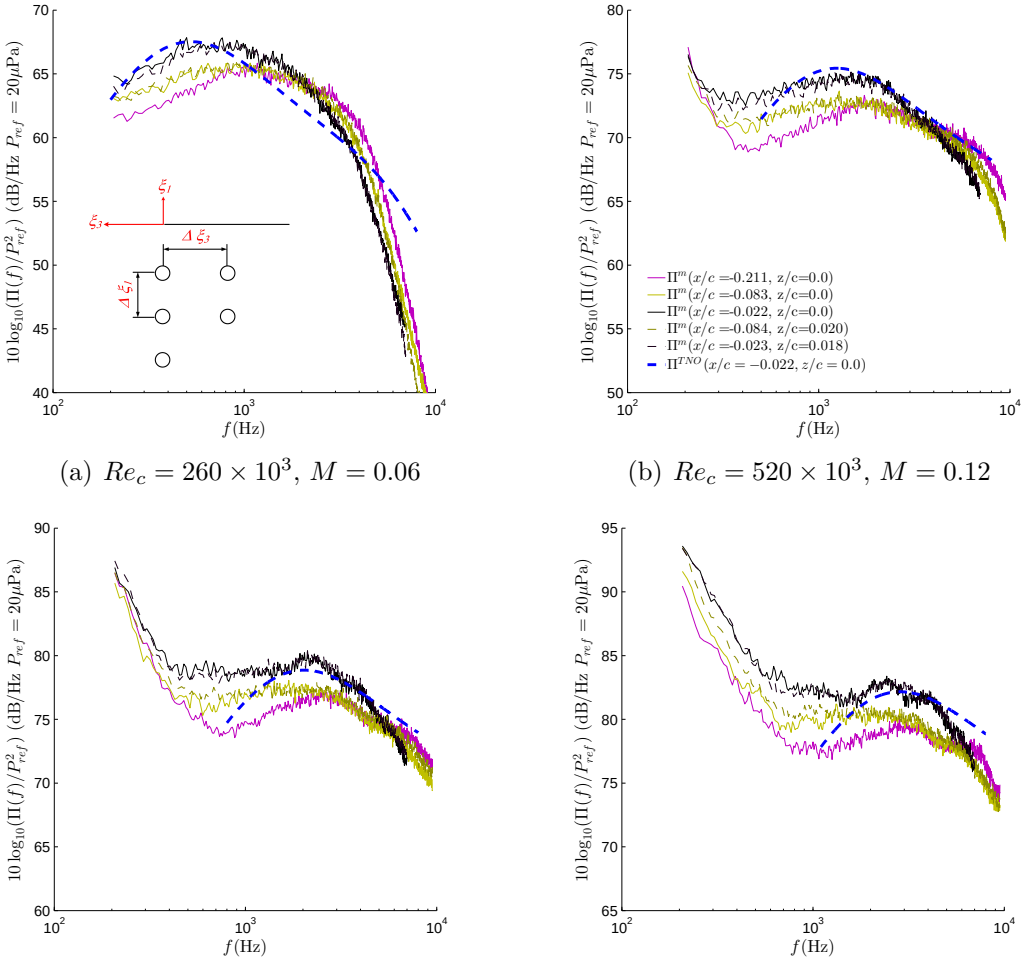

(a) $Re_c = 260 \times 10^3$, $M = 0.06$

(b) $Re_c = 520 \times 10^3$, $M = 0.12$

(c) $Re_c = 780 \times 10^3$, $M = 0.18$

(d) $Re_c = 1040 \times 10^3$, $M = 0.23$

Figure 7: Evaluation of the measured and predicted wall-pressure frequency spectra $\Pi(f)$ along the chord. The superscripts m and TNO indicate measured and predicted with TNO model spectra, respectively.

given by Eq.(42). Previous coherence measurements on airfoil [2, 51, 50, 41] have yielded similar values of b_c for a similar range of velocities, flow conditions and on symmetrical and non-symmetrical airfoils.

Single point wall pressure spectra

Figure 7 shows the variation in surface pressure power spectral density for five remote microphones. Three remote microphones are located along the streamwise direction between $0.63 < x_1/c < 0.98$, while two of the five mi-

crophones are positioned at spanwise position $z/c = 0.02$(relative to the mid-chord), as shown in Figure 7(a). In this configuration two pair of microphones are positioned in the same streamwise position. These two pairs experience similar surface spectra.

As the trailing edge is approached the spectra rotate in the sense that low frequencies decay while high frequencies increase. The peak-frequency is also observed to reduce as the TE is approached due to the increase in the boundary layer scales owing to a thickening of the boundary caused by the adverse pressure gradient. This trend is clearly seen at $U_\infty = 20m/s$, corresponding to $Re_c = 260 \times 10^3$ and $M = 0.06$. At very low frequencies, however, the pressure is dominated by jet noise. The peak frequency, which roughly equals $\bar{U}_c/\delta$, increases as flow speed is increased.

Comparison of airfoil self-noise prediction scheme with measurements

Figure 8 shows a comparison between self-noise predictions and measurements at the four flow speeds of $U_\infty = 20\,\mathrm{m/s}$, $40\,\mathrm{m/s}$, $60\,\mathrm{m/s}$, $80\,\mathrm{m/s}$. The measured spectra were corrected for shear-layer refraction following the method proposed by Amiet [25]. Two predictions are presented. The first, $S_{pp}^{Amiet}(\Pi^{TNO})$, is based on Eq.(1), and includes a prediction of the surface pressure spectrum as described by Eq.(28). The second, $S_{pp}^{Amiet}(\Pi^{m})$, is based on Eq.(1) but uses measurements of the surface pressure spectra plotted in Figure 7 using the microphone positioned closest to the trailing edge (at $x/c = -0.02$), and the spanwise length-scale estimated from Eq.(43). In this figure far-field acoustic pressure measurements were acquired with a microphone positioned at $r_m = 1.17\,\mathrm{m}$ and $\phi_m = 95°$.

At the two lowest speeds (20 m/s and 40 m/s), agreement between measurements and both predictions are generally within 2 dB over the entire frequency range. Also shown in these figures are the predictions obtained using the empirical prediction method developed by Brooks [2] to predict the sound pressure level spectrum of the radiated noise by a NACA-0012 airfoil of arbitrary chord, frequency, angle of attack and flow speed. Whilst the Brooks prediction captures the general trend in the spectrum, spectral details are clearly not able to be captured.

At the two highest speeds (60 m/s and 80 m/s), however, both predictions are in very close agreement but underestimate the measured spectra by about 2dB, with the error at the highest speed being slightly greater than at 60 m/s. at all four speeds, however, spectral shape, including oscillations due to non-compactness effects, is well captured.

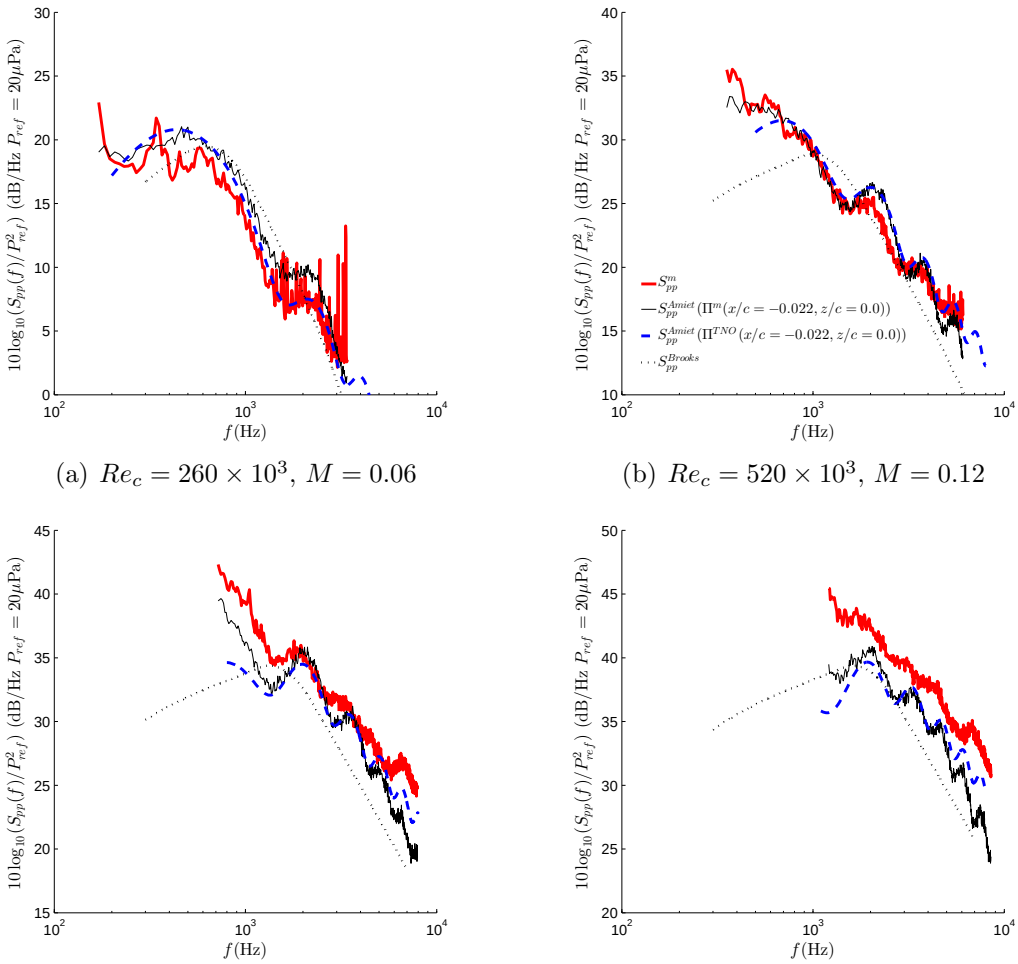

(a) $Re_c = 260 \times 10^3$, $M = 0.06$

(b) $Re_c = 520 \times 10^3$, $M = 0.12$

(c) $Re_c = 780 \times 10^3$, $M = 0.18$

(d) $Re_c = 1040 \times 10^3$, $M = 0.23$

Figure 8: Evaluation of the measured and predicted far-filed sound pressure level $S_{pp}(f)$. Prediction of the far-field SPL is based on TNO and Amiet models. The superscripts m indicated measures SPL, and superscripts *Amiet* and *Brooks* indicate Amiet far-field trailing edge model and Brook's [16] empirical formulas, respectively.

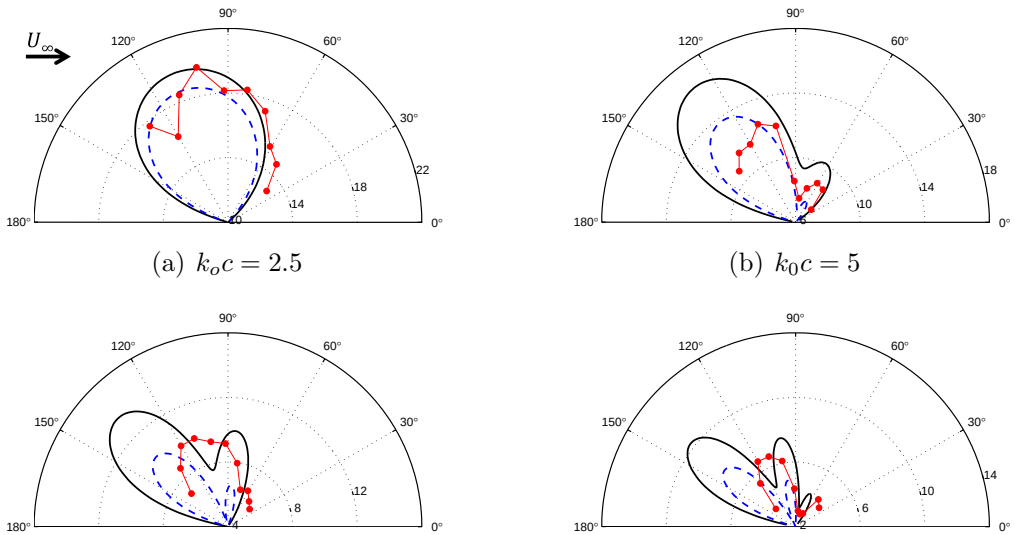

(a) $k_o c = 2.5$

(b) $k_0 c = 5$

(c) $k_0 c = 7.5$

(d) $k_0 c = 10$

Figure 9: Comparison of measured versus predicted polar SPL directivity patterns for four reduced frequencies $k_0 c$ at $Re_c = 260 \times 10^5$, corresponding to $M = 0.06$. SPL levels are plotted in dB and the color scheme is equivalent to the one presented in Figure 8.

Far-field self-noise sound pressure level directivity

In this section we compare measurements and predictions of the far field directivity in decibels using the two prediction methods under discussion. Figures 9- 11 show a comparison of the measured far-field airfoil self-noise directivity plots for three flow speeds $U_\infty = 20\,\mathrm{m/s}$, $40\,\mathrm{m/s}$, and $60\,\mathrm{m/s}$. Each figure contains four directivity plots corresponding to four non-dimensional acoustic frequencies $k_0 c = 2.5$, 5, 7.5 and 10.

Once again we observe good agreement between the two prediction methods. Agreement with experiment is generally better than 2 dB at most downstream angles for almost all frequencies and flow speeds under consideration. Agreement is less good at upstream radiation angles due to diffraction of the airfoil noise by the nozzle. The same phenomenon was previously observed by Moreau et al. [52]. The directivity patterns can be observed to vary between a compact lift dipole to that of a semi-infinite half-plane as non-dimensional acoustic frequency is increases, thereby highlighting the importance of including finite chord effects in the airfoil self-noise prediction.

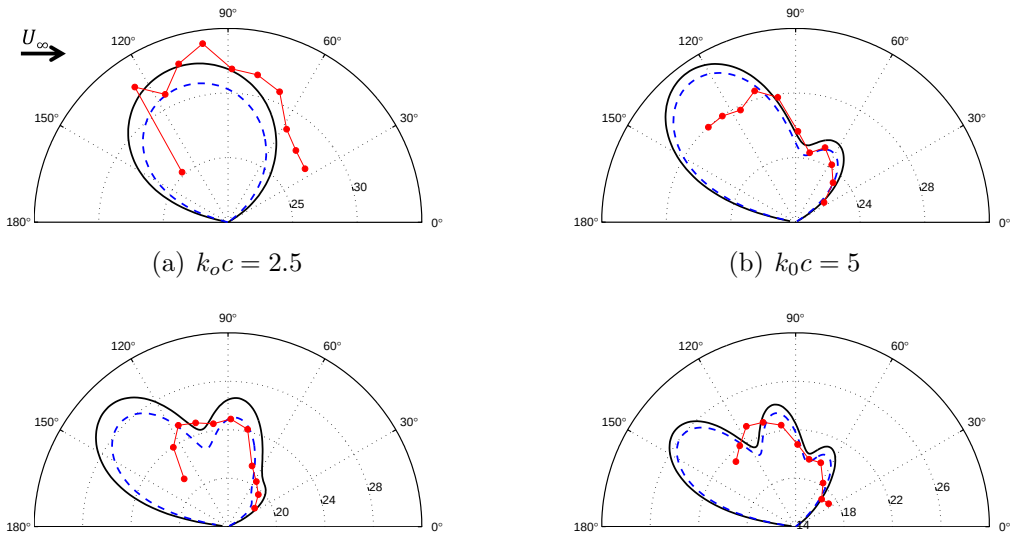

(a) $k_o c = 2.5$ (b) $k_0 c = 5$

(c) $k_0 c = 7.5$ (d) $k_0 c = 10$

Figure 10: Comparison of measured versus predicted polar SPL directivity patterns for four reduced frequencies $k_0 c$ at $Re_c = 520 \times 10^5$, corresponding to $M = 0.12$. SPL levels are plotted in dB and the color scheme is equivalent to the one presented in Figure 8.

6 Sensitivity study of noise prediction to model parameters

In this section we explore the sensitivity of the surface pressure Π and far field S_{pp} noise prediction to the main parameters of the model, namely the stretching coefficients β_1 and β_3 and $\Lambda_{2|22}$, the vertical integral length scale.

Figure 12 illustrates the sensitivity of the far field and surface pressure predictions to the stretching coefficients β_1 and β_3 at $U_\infty = 40\,\mathrm{m/s}$ (corresponding to $Re_c = 520 \times 10^3$). In this figures are the spectral predictions for the beta ratio $\beta_2/\beta_1 = 1/2$ and $\beta_3/\beta_1 = 3/4$ assumed in this study and for $\beta_2/\beta_1 = \beta_3/\beta_1 = 1$, when isotropy is assumed. The difference on both surface and far field spectra are less than 1 dB suggesting that the turbulence anisotropy, at least as represented in the current formulation of Eq.39, has only a comparatively weak effect. The current formulation is chosen to preserve kinetic energy. It is possible than an alternative anistropic turbulence spectral model, such has the one by Kirschen[53], will exhibit a stronger sensitivity to turbulence anisotropy.

The vertical integral length scale $\Lambda_{2|22}$ on the other hand has more pronounced effect as it appears explicitly in Eq.(28) and implicitly in definition

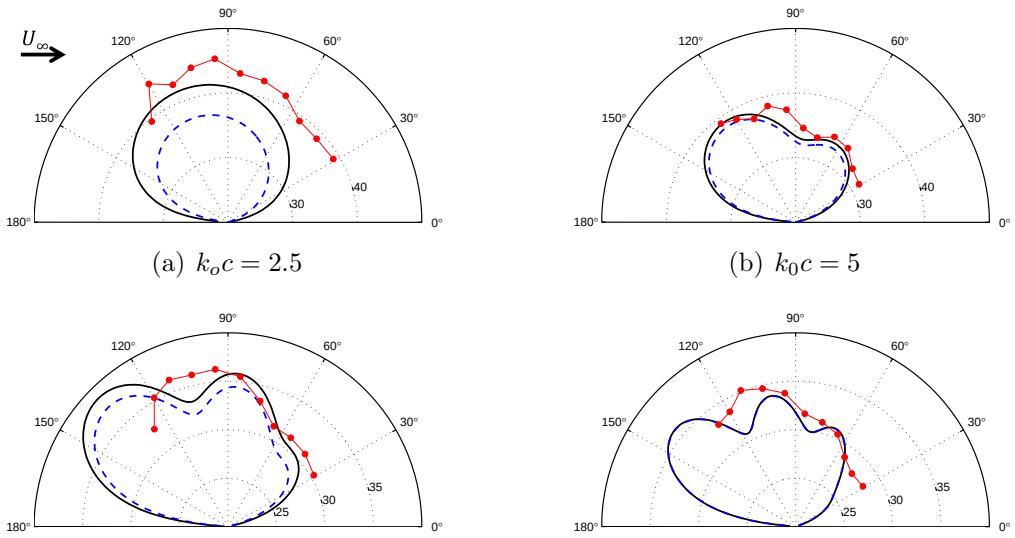

(a) $k_o c = 2.5$ (b) $k_0 c = 5$

(c) $k_0 c = 7.5$ (d) $k_0 c = 10$

Figure 11: Comparison of measured versus predicted polar SPL directivity patterns for four reduced frequencies $k_0 c$ at $Re_c = 780 \times 10^5$, corresponding to $M = 0.18$. SPL levels are plotted in dB and the color scheme is equivalent to the one presented in Figure 8.

of k_e.

Figure 13 shows the sensitivity of the prediction model to $\Lambda_{2|22}$. Surface pressure Π and far-field pressure spectra S_{pp} at $U_\infty = 40\,\mathrm{m/s}$ (corresponding to $Re_c = 520 \times 10^3$) is shown for two additional corrected vertical integral length scales. The corrected integral length scale is defined as following $\Lambda'_{2|22} = \alpha \Lambda_{2|22}$, where α is a factor used here to vary the integral length scale $\Lambda_{2|22}$ in order to assess how sensitive the predicted surface and far field pressure to small perturbations to its value. Increasing alpha between 0.75 to 1.25 causes both spectral levels to drop, with low frequencies exhibiting a greater sensitivity to alpha than at high frequencies. Level differences are nearly 10 dB at low frequencies dropping to 5 dB at the highest frequency of interest. Most of this sensitivity originates from the behaviour of the velocity spectrum defined by Eq.39. Clearly, therefore, accurate noise predictions requires the length-scale to determined accurately whereas the extent of anisotropy of the turbulent boundary layer is less important.

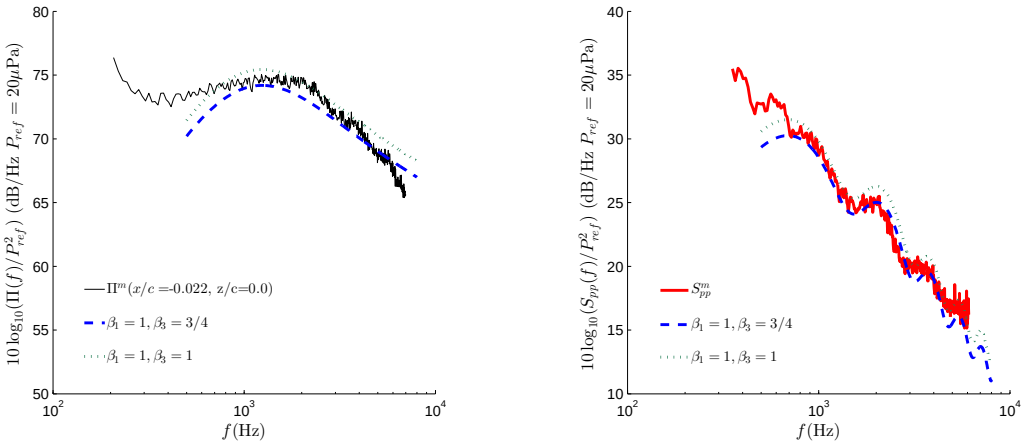

(a) (b)

Figure 12: Effect of stretching factors β_i on prediction of the surface pressure Π and far-field pressure S_{pp} at $U_\infty = 40\,\mathrm{m/s}$ (corresponding to $Re_c = 520 \times 10^3$).

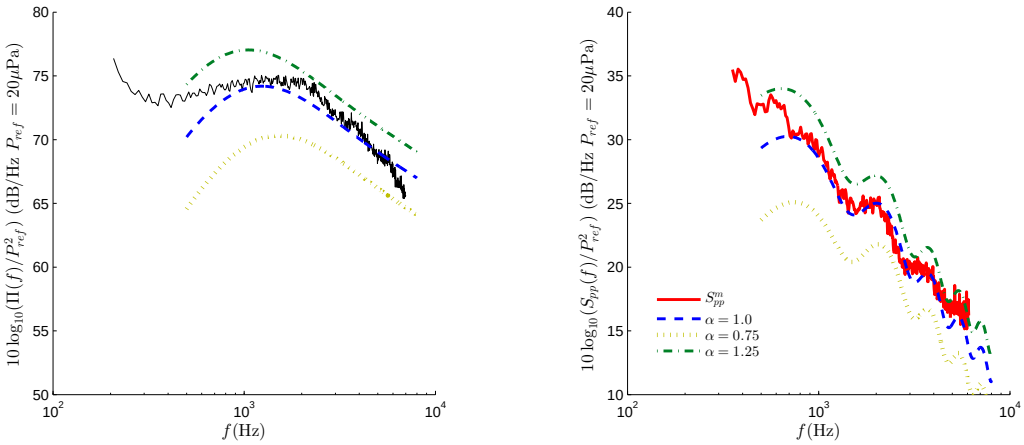

(a) (b)

Figure 13: Effect of $\Lambda_{2|22}$ on prediction of the surface pressure Π and far-field pressure S_{pp} at $U_\infty = 40\,\mathrm{m/s}$ (corresponding to $Re_c = 520 \times 10^3$).

7 Discussion and conclusions

In the current work we further develop the two-step TNO-Blake airfoil self-noise prediction model. In the first step the surface pressure wavenumber-frequency spectrum under a turbulent boundary-layer is described by the Blake model. In the second step the sound radiation to the far-field is described with the Amiet trailing edge broadband noise model.

To increase the accuracy in prediction of the wavenumber-frequency spectrum and avoid tuning of the model parameters we only make use of empirical functions. One of the main contributions of this work is the use of recent work of Alfredsson to estimate the variation of mean square turbulence velocity as a function of the mean streamwise velocity profile. We set the ratios of mean square velocities to those of an incompressible zero pressure gradient boundary-layer, i.e. in the following empirical ratios $\overline{u_2^2} = \frac{1}{2}\overline{u_1^2}$ and $\overline{u_3^2} = \frac{3}{4}\overline{u_1^3}$ [42]. The validity of the Alfreddson function was validated by measuring boundary-layer profile upstream of the trailing edge. The anisotropy in the von-Kármán velocity spectra is based on empirical ratios between wall normal, streamwise, and spanwise velocity components.

The Amiet radiation model replaces the infinite half-plane assumption employed in the original Blake-TNO model and takes into the account the finite length of the airfoil chord. The improved TNO-Amiet model captures accurately the overall level within less than 2 dB. Far-field spectra predicted with the TNO-Amiet model captures the oscillation in the spectrum in the mid-frequency range.

For large wind-turbine blades the assumption of semi-infinite chord can represent the underlying physics. However, the development of prediction models is based on experiments conducting with scaled models. Thus, it is essential to take the finite chord length of the model into the account when comparing the experimental data to the one predicted by the theory. The Amiet model is therefore incorporated in the prediction scheme. The Amiet theory allows to capture the shape of the radiated far-field spectra, and is in good agreement with the experimental results, particularly in the low-frequency range. A slight deviation between the measured and predicted values is observed at high-frequency range. One reason to this deviation could be that the high-frequency range is dominated by a contribution from the energy associated with the dissipation frequency range. The other reason could be a result of frozen turbulence assumption that gives a better approximation at low-frequency range [54]. The predicted and measured far-field trailing edge noise spectra scales classically with U^5 (not shown here).

The key to successful prediction of the far-field self-noise levels is not necessary an accurate prediction of surface pressure spectrum $\Pi(\omega)$ but rather

accurate prediction the wavenumber-frequency spectrum $\hat{\mathscr{P}}_w(k_1, k_3 = 0, \omega)$. The current work extends the so called TNO model to include recent advances in scaling of turbulent streamwise intensities with established assumption that wall-normal intensity is about half of the streamwise intensity. The wavenumber-frequency spectrum is particularly sensitive to $\Lambda_{2|22}$. It is less dependent on the β_i anisotropic stretching parameters.

It should be noted that the current model is valid for arbitrary airfoil geometries at low angles of attack and with small gradients in streamwise and spanwise directions. The model is highly sensitive to $\Lambda 2|22$ is it appears explicitly in Eq.(28) and implicitly in the definition of wavenumber of energy berrying eddies. However further investigation are required for various airfoil geometries and angles of attack.

References

[1] G.P. Van den Berg, E. Pedersen, J. Bouma, and R. Bakker. Project wind-farm perception: visual and acoustic impact of wind turbine farms on residents. *Final report, June*, 3(2008):63, 2008.

[2] T. F. Brooks, D. S. Pope, and M. A. Marcolini. *Airfoil self-noise and prediction*, volume 1218. National Aeronautics and Space Administration, Office of Management, Scientific and Technical Information Division, 1989.

[3] A. A. Powell. Aerodynamic noise and the plane boundary. *The Journal of the Acoustical Society of America*, 32(8):982–990, 1960.

[4] J. E. Williams and L. H. Hall. Aerodynamic sound generation by turbulent flow in the vicinity of a scattering half plane. *Journal of Fluid Mechanics*, 40(04):657–670, 1970.

[5] M. J. Lighthill. On sound generated aerodynamically. i. general theory. *Proceedings of the Royal Society of London. Series A. Mathematical and Physical Sciences*, 211(1107):564–587, 1952.

[6] K. L. Chandiramani. Diffraction of evanescent waves, with applications to aerodynamically scattered sound and radiation from unbaffled plates. *The Journal of the Acoustical Society of America*, 55(1):19–29, 1974.

[7] D. M. Chase. Sound radiated by turbulent flow off a rigid halfplane as obtained from a wavevector spectrum of hydrodynamic pressure. *The Journal of the Acoustical Society of America*, 52(3B):1011–1023, 1972.

[8] D. M. Chase. Noise radiated from an edge in turbulent flow. *AIAA Journal*, 13(8):1041–1047, 1975.

[9] R. K. Amiet. Noise due to turbulent flow past a trailing edge. *Journal of Sound and Vibration*, 47(3):387–393, 1976.

[10] R. K. Amiet. Effect of the incident surface pressure field on noise due to turbulent flow past a trailing edge. *Journal of Sound and Vibration*, 57(2):305–306, 1978.

[11] M. Roger and S. Moreau. Back-scattering correction and further extensions of amiet's trailing-edge noise model. part 1: theory. *Journal of Sound and Vibration*, 286(3):477–506, 2005.

[12] M. S. Howe. Edge-source acoustic greens function for an airfoil of arbitrary chord, with application to trailing-edge noise. *The Quarterly Journal of Mechanics and Applied Mathematics*, 54(1):139–155, 2001.

[13] R. H. Kraichnan. Pressure fluctuations in turbulent flow over a flat plate. *The Journal of the Acoustical Society of America*, 28(3):378–390, 1956.

[14] W. K. Blake. *Mechanics of Flow-Induced Sound and Vibration V2: Complex Flow-Structure Interactions*, volume 2. Elsevier, 2012.

[15] R. R. Parchen and Technisch Physische Dienst TNO-TH. *Progress report DRAW: A prediction scheme for trailing edge noise based on detailed boundary layer characteristics*. TNO Report HAG-RPT-980023, TNO Institute of Applied Physics, 1998.

[16] T.F. Brooks and T.H. Hodgson. Trailing edge noise prediction from measured surface pressures. *Journal of Sound and Vibration*, 78(1):69–117, 1981.

[17] M. Kamruzzaman, Th. Lutz, A. Herrig, and E. Kraemer. Rans based prediction of airfoil trailing edge far-field noise: Impact of isotropic & anisotropic turbulence. In *Proceedings of the 14th AIAA/CEAS Aeroacoustics Conference, Vancouver, Canada, AIAA Paper*, number 2008-2867, 2008.

[18] A. Wolf, Th. Lutz, W. Würz, E. Krämer, O. Stalnov, and A. Seifert. Trailing edge noise reduction of wind turbine blades by active flow control. *Wind Energy*, 2014.

[19] Th. Lutz, A. Herrig, E. Würz, M. Kamruzzaman, and E. Krämer. Design and wind-tunnel verification of low-noise airfoils for wind turbines. *AIAA Journal*, 45(4):779–785, 2007.

[20] A. Herrig, W. Würz, Th. Lutz, and E. Krämer. Trailing-edge noise measurements using a hot-wire based coherent particle velocity method. In *24th AIAA Applied Aerodynamics Conference, San Francisco, California*, number 2006-3876, 2006.

[21] F. Bertagnolio, A. Fischer, and W. J. Zhu. Tuning of turbulent boundary layer anisotropy for improved surface pressure and trailing-edge noise modeling. *Journal of Sound and Vibration*, 333(3):991 – 1010, 2014.

[22] M. Drela and M.B. Giles. Viscous-inviscid analysis of transonic and low reynolds number airfoils. *AIAA Journal*, 25(10):1347–1355, 1987.

[23] T. P. Chong, P.F. Joseph, and P. O. A. L. Davies. A parametric study of passive flow control for a short, high area ratio 90 deg curved diffuser. *Journal of Fluids Engineering*, 130(11), 2008.

[24] T. P. Chong, P. F. Joseph, and P. O. A. L. Davies. Design and performance of an open jet wind tunnel for aero-acoustic measurement. *Applied Acoustics*, 70(4):605–614, 2009.

[25] R. K. Amiet. Refraction of sound by a shear layer. *Journal of Sound and Vibration*, 58(4):467–482, 1978.

[26] R. H. Schlinker and R. K. Amiet. Helicopter rotor trailing edge noise. In *NASA CR-3470*, volume 1, 1981.

[27] G. Batchelor. *An Introduction to Fluid Dynamics*. Cambridge University Press, 1967.

[28] H. Lamb. *Hydrodynamics*. Dover, New York, 1945.

[29] J. E. F. Williams. Surface-pressure fluctuations induced by boundary-layer flow at finite mach number. *Journal of Fluid Mechanics*, 22(03):507–519, 1965.

[30] G. M. Lilley. *Pressure fluctuations in an incompressible turbulent boundary layer*. College of Aeronautics, 1960.

[31] J. E. F. Williams. The noise from turbulence convected at high speed. *Philosophical Transactions for the Royal Society of London. Series A, Mathematical and Physical Sciences*, pages 469–503, 1963.

[32] M. Drela and M.B. Giles. Ises: A two-dimensional viscous aerodynamic design and analysis code. pages 1–12. Springer, 1989.

[33] P. Moriarty. Nafnoise: a program for calculating 2d airfoil noise. *Design Code, National Wind Technology Center, USA*, 2003.

[34] F. Bertagnolio, H. Aagaard Madsen, and C. Bak. Comparison and validation of trailing edge noise models. In 3rd *International Conference on Wind Turbine Noise*, 2009.

[35] F. Bertagnolio. *Trailing edge noise model applied to wind turbine airfoils.* Forskningscenter Risø Roskilde, 2008.

[36] Th. Lutz, A. Herrig, W. Würz, K. Braun, and E. Krämer. Constrained aerodynamic & aeroacoustic design of wind-rotor airfoils. In *First International Meeting on Wind Turbine Noise: Perspectives for Control, Berlin*, pages 17–18, 2005.

[37] Th. Lutz, W. Würz, A. Herrig, K. Braun, and S. Wagner. Numerical optimization of silent airfoil sections. In 7th *German Wind Energy Conference Proceedings*, 2004.

[38] G. Guidati and S. Wagner. Design of reduced noise airfoils for wind turbines. In *Proc. of the ECCOMAS 2000 Conference, Barcelona, Spain*, 2000.

[39] D. Coles. The law of the wake in the turbulent boundary layer. *Journal of Fluid Mechanics*, 1(02):191–226, 1956.

[40] J. Hinze. Turbulence, 1972.

[41] A. G. Sagrado. *Boundary layer and trailing edge noise sources.* PhD thesis, University of Cambridge, 2007.

[42] D. C. Wilcox. *Turbulence modeling for CFD*, volume 2. DCW industries La Canada, CA, 1998.

[43] P. S. Klebanoff. *Characteristics of turbulence in a boundary layer with zero pressure gradient.* National Advisory Committee for Aeronautics, 1955.

[44] M. M. Gibson, C. A. Verriopoulos, and N. S. Vlachos. Turbulent boundary layer on a mildly curved convex surface. *Experiments in Fluids*, 2(1):17–24, 1984.

[45] P. Henrik Alfredsson, Antonio Segalini, and Ramis Örlü. A new scaling for the streamwise turbulence intensity in wall-bounded turbulent flows and what it tells us about the outer peak. *Physics of Fluids (1994-present)*, 23(4):–, 2011.

[46] P. H. Alfredsson, R. Örlü, and A. Segalini. A new formulation for the streamwise turbulence intensity distribution. In *Journal of Physics: Conference Series*, volume 318, page 022002. IOP Publishing, 2011.

[47] H. Schlichting, K. Gersten, and K. Gersten. *Boundary-layer theory*. Springer, 2000.

[48] M. Kamruzzaman, A. Herrig, Th. Lutz, W. Würz, E. Krämer, and S. Wagner. Comprehensive evaluation and assessment of trailing edge noise prediction based on dedicated measurements. *Noise Control Engineering Journal*, 59(1):54–67, 2011.

[49] R. L. Panton and J. H. Linebarger. Wall pressure spectra calculations for equilibrium boundary layers. *Journal of Fluid Mechanics*, 65(02):261–287, 1974.

[50] G. M. Corcos. The structure of the turbulent pressure field in boundary-layer flows. *Journal of Fluid Mechanics*, 18(03):353–378, 1964.

[51] M. Roger and S. Moreau. Broadband self noise from loaded fan blades. *AIAA Journal*, 42(3):536–544, 2004.

[52] S. Moreau, C. Schram, and M. Roger. Diffraction effects on the trailing-edge noise measured in an open-jet anechoic wind tunnel. In *13th AIAA/CEAS Aeroacoustics Conference, Rome, Italy, AIAA Paper*, number 2007-3706, 2007.

[53] E E. Kerschen and P P Gliebe. Fan noise caused by the ingestion of anisotropic turbulence-a model based on axisymmetric turbulence theory. In *6th AIAA Aeroacoustics Conference*, 1980.

[54] Q. Zhou and P. Joseph. A frequency domain numerical method for airfoil broadband self-noise prediction. *Journal of Sound and Vibration*, 299(3):504–519, 2007.